Chapter 5

Nanoparticle aggregation kinematics on the quadratic convective MHD flow of nanomaterial past an inclined flat plate with sensitivity analysis *

5.1 Introduction

Ethylene glycol-based nanofluid containing titanium dioxide is frequently used in cooling processes, solar collectors, and nuclear reactors. Oxides are chemically more stable than metal nanoparticles as metals oxidise easily. Also, ethylene glycol is more preferable since it can be used over a wide temperature range. Furthermore, TiO_2 is a harmless material and is widely available making the nanoparticle suitable for various thermal applications. Motivated by experimental results and practical applicability, a nanofluid prepared by dispersing TiO_2 nanoparticles in ethylene glycol is used for this theoretical study. The main objectives of the current study are to:

- Study the quadratic convective flow of nanofluid over an inclined plate.
- Investigate the significance of aggregation of nanoparticles on the heat transfer.
- Compare the results for two different geometries, viz., vertical plate and inclined plate.
- Analyze and optimize the heat transfer rate using the Response Surface Methodology.
- Explore the sensitivity of heat transfer rate with respect to the governing

*Published in: Proceedings of the Institution of Mechanical Engineers, Part E (Sage Publications Ltd), 2021; 236 (3)

operational parameters.

5.2 Mathematical Formulation

The physical model of the present problem is described in Fig. 5.1. Consider a two-dimensional steady flow of ethylene glycol-based titania nanofluid past a flat plate at $y = 0$ with an angle of inclination α towards the vertical. The constant value of temperature is chosen as T_w, at the plate ($y = 0$) and the ambient value is T_∞, far from the plate ($y \to \infty$). The aggregation kinematics of the nanoparticles is included in the model. A variable magnetic field of intensity ${B_x}^2 = B_0^2 x^{-0.5}$ (B_0-uniform magnetic field) is applied perpendicular to the fluid flow. An exponential space-based heat source ($Q_1 = Q_e x^{-0.5}$) and radiative heat flux are accounted in the system. The viscous and Joule heating effects are negligible and hence are not considered. Under nonlinear Boussinesq and boundary layer approximations, the flow can be described by the following governing equations (Kuznetsov & Nield, 2014),(Acharya, Das, & Kundu, 2017),(Goyal & Bhargava, 2018):

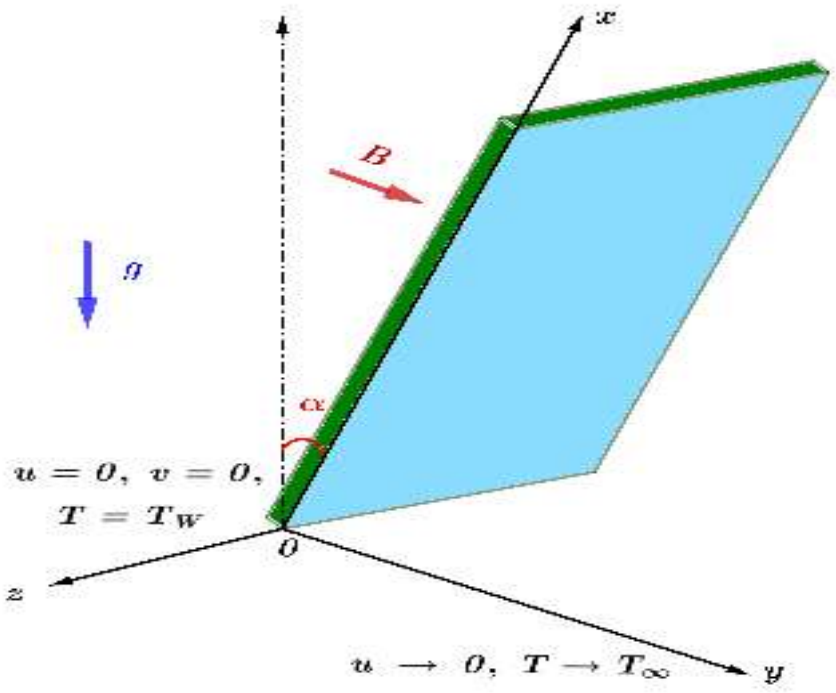

Figure 5.1: *Physical configuration.*

$$\frac{\partial u}{\partial x} + \frac{\partial v}{\partial y} = 0 \tag{5.2.1}$$

$$\rho_{nf}\left(u\frac{\partial u}{\partial x}+v\frac{\partial u}{\partial y}\right)= \mu_{nf}\frac{\partial^2 u}{\partial y^2}+\rho_{nf}g\left\{(\beta_0)_{nf}(T-T_\infty)+(\beta_1)_f(T-T_\infty)^2\right\}\cos\alpha -\sigma_{nf}B^2u \tag{5.2.2}$$

$$(\rho C_p)_{nf}\left(u\frac{\partial T}{\partial x}+v\frac{\partial T}{\partial y}\right)=k_{nf}\frac{\partial^2 T}{\partial y^2}-\frac{\partial q_R}{\partial y} +Q_1(T_w-T_\infty)\exp\left[-m\left\{\frac{(\beta_0)_f g(T_w-T_\infty)}{v_f\alpha_f}\right\}^{\frac{1}{4}}\frac{y}{x^{\frac{1}{4}}}\right] \tag{5.2.3}$$

Appropriate boundary conditions are

$$\begin{aligned}\text{At } y=0: &\quad u=0,\quad v=0,\quad T=T_w\\ \text{As } y\to\infty: &\quad u\to 0,\quad T\to T_\infty.\end{aligned} \tag{5.2.4}$$

where, u, v are the velocity components in the x and y directions, T is the temperature of the liquid. $T_w,\ T_\infty$- are the temperatures at the plate and ambient conditions, g is the acceleration due to gravity, α is the inclination of the plate, B is the magnetic flux, q_R is the radiative heat flux, Q_1 is the exponential heat source coefficient, m is the exponential index, ρ, μ and k are respectively the density, dynamic viscosity and thermal conductivity. β_0 and β_1 are the first and second order thermal expansion coefficients, α_f, C_p, and ν_f are respectively the thermal diffusivity, specific heat and kinematic viscosity.

The radiative heat flux for the optically thick fluid in this study is approximated using the Rosseland equation as follows:

$$q_R=-\frac{4\sigma^*}{3k^*}\frac{\partial T^4}{\partial y},\qquad T^4\approx 4T_\infty^3T-3T_\infty^4. \tag{5.2.5}$$

Here σ^* is the Stefan-Boltzmann constant and k^* is the mean absorption factor. The conventional Maxwell model for thermal conductivity and the Brinkman model for viscosity deviate significantly from the experimental data and hence lack accuracy. Therefore, thermophysical properties of nanofluid with the influence of nanoparticle aggregation are used as described in Table 5.1 and thereafter. Nanofluids are characterized by higher viscosity and thermal conductivity which is due to the aggregation kinematics of nanoparticles. A more suitable and realistic model including aggregation effects for the viscosity of $EG-TiO_2$ nanofluid is the modified

Table 5.1: *Thermophysical properties of the nanofluid with aggregation (Mackolil & Mahanthesh, 2021b)*

Effective density	$\frac{\rho_{nf}}{\rho_f} = (1-\phi_a) + \phi_a \frac{\rho_s}{\rho_f} = A_1$
Effective heat capacity	$\frac{(\rho C_p)_{nf}}{(\rho C_p)_f} = (1-\phi_a) + \phi_a \frac{(\rho C_p)_s}{(\rho C_p)_f} = A_2$
Effective thermal expansion	$\frac{(\rho\beta_0)_{nf}}{(\rho\beta_0)_f} = (1-\phi_a) + \phi_a \frac{(\rho\beta_0)_s}{(\rho\beta_0)_f} = A_3$
Effective electrical conductivity	$\frac{\sigma_{nf}}{\sigma_f} = 1 + \frac{3\left(\frac{\sigma_s}{\sigma_f}-1\right)\phi_a}{\left(\frac{\sigma_s}{\sigma_f}+2\right)-\left(\frac{\sigma_s}{\sigma_f}-1\right)\phi_a} = A_4$

Krieger-Dougherty model (Chen et al., 2007) as given below:

$$\frac{\mu_{nf}}{\mu_f} = \left(1 - \frac{\phi_a}{\phi_m}\right)^{[\eta]\phi_m} = A_5, \quad \phi_a = \phi\left(\frac{r_a}{r_p}\right)^{3-D}, \tag{5.2.6}$$

An experimentally agreed value of the relative radii of the aggregates to the individual nanoparticle, $\frac{r_a}{r_p}$ is 3.34 by assuming the shape of the aggregate as spherical and D is 1.8. The value of ϕ_m is 0.605 and $[\eta]$ is 2.5 (see (Chen et al., 2007)).
The effective thermal conductivity is modeled by combining the Maxwell and Bruggeman models to incorporate the aggregation aspect for $EG - TiO_2$ nanofluid (Chen et al., 2007). The model is given below:

$$\frac{k_{nf}}{k_f} = \frac{(k_a + 2k_f) - 2\phi_a(k_f - k_a)}{(k_a + 2k_f) + \phi_a(k_f - k_a)} = A_6, \tag{5.2.7}$$

$$\frac{k_a}{k_f} = \frac{1}{4}\left\{(3\phi_{in}-1)\frac{k_s}{k_f} + (3(1-\phi_{in})-1) + \left[\left((3\phi_{in}-1)\frac{k_s}{k_f} + (3(1-\phi_{in})-1)\right)^2 + 8\frac{k_s}{k_f}\right]^{\frac{1}{2}}\right\} \tag{5.2.8}$$

, $\phi_{in} = \left(\frac{r_a}{r_p}\right)^{D-3}$,where ϕ_{in} denotes the solid volume fraction of aggregates.
Thermophysical properties of nanoparticles and base fluid at 300 K are shown in the table 5.2

The following similarity variables (Kuznetsov & Nield, 2010) are used in the computation procedure:

$$\left.\begin{aligned} \zeta = \frac{y}{x} Ra_x^{\frac{1}{4}}, Ra_x = \frac{(\beta_0)_f \; g(T_w - T_\infty)x^3}{\nu_f \alpha_f}, \\ S(\zeta) = \frac{\psi}{\alpha_f Ra_x^{\frac{1}{4}}}, \theta(\zeta) = \frac{T - T_\infty}{T_w - T_\infty}. \end{aligned}\right\} \tag{5.2.9}$$

Table 5.2: *Thermo physical properties of base fluid and nanoparticles at* $300K$ *(Mackolil & Mahanthesh, 2021b)*

Model	$\rho\,(kgm^{-3})$	$C_p\,(Jkg^{-1}K^{-1})$	$k\,(Wm^{-1}K^{-1})$	$\beta\times10^{-5}\,(K^{-1})$	$\sigma\,(s/m)$
TiO_2	4250	686.2	8.9538	0.9	2.38×10^{6}
EG	1114	2415	0.252	57	1.07×10^{-6}

Here, ψ is the stream function with

$$u=\frac{\partial\psi}{\partial y}\ \ ,\ \ v=-\frac{\partial\psi}{\partial x}. \tag{5.2.10}$$

Using the similarity variables, Eqns. (5.2.1) to (5.2.3) become,

$$S'''-\frac{1}{4Pr_f}\frac{A_1}{A_5}\left(2(S')^2-3SS''\right)+\frac{1}{A_5}\left\{A_3\theta+A_1\alpha_1\theta^2\right\}cos\alpha-\frac{A_4}{A_5}MS'=0, \tag{5.2.11}$$

$$\theta''\left(1+\frac{4}{3}\frac{R}{A_6}\right)+\frac{Q_E}{A_6}\exp\left(-m\zeta\right)+\frac{3}{4}\frac{A_2}{A_6}\,S\theta'=0, \tag{5.2.12}$$

The reduced boundary conditions are

$$\left.\begin{array}{c} S'(0)=0, S(0)=0, \theta(0)=1. \\ S'(\infty)\to0, \theta(\infty)\to0. \end{array}\right\} \tag{5.2.13}$$

The non-dimensional parameters are given below:

$$\begin{array}{c} \alpha_1=\frac{\beta_{1f}}{\beta_{0f}}\left(T_w-T_\infty\right), Pr_f=\frac{\nu_f}{\alpha_f},\ R=\frac{4\sigma^*T_\infty^3}{k^*k_f}, \\ M=\frac{\sigma_f B_0^2\left(\nu_f\alpha_f\right)^{0.5}}{\mu_f\left(g(\beta_0\ )_f(T_w-T_\infty)\right)^{0.5}},\ Q_E=\frac{Q_e\left(\nu_f\alpha_f\right)^{0.5}}{k_f\left(g(\beta_0\ )_f(T_w-T_\infty)\right)^{0.5}}. \end{array} \tag{5.2.14}$$

where, α_1 (quadratic thermal convection parameter), Pr_f (Prandtl number), R (radiation parameter), M (Hartmann number), and Q_E (exponential heat source parameter).

Thermal nanofluidic devices depend on the physical quantities such as skin friction and the rate of heat transfer. The information regarding these physical quantities plays a crucial part for designing highly efficient nanofluidic devices. The local

skin friction coefficient and local Nusselt number is defined as follows (Kandasamy, Dharmalingam, & Prabhu, 2018),(Kuznetsov & Nield, 2010),(Aladdin, Bachok, & Pop, 2020):

$$C_f = \frac{\tau_w}{\rho_f u_w^2}, Nu = \frac{x q_w}{k_f \left(T_w - T_\infty\right)}. \tag{5.2.15}$$

where τ_w and q_w are the wall shear stress and the heat flux respectively which are defined as follows:

$$\tau_w = \mu_{nf}\left(\frac{\partial u}{\partial y}\right)_{y=0}, q_w = -\left(k_{nf}\frac{\partial T}{\partial y} - q_R\right)_{y=0}. \tag{5.2.16}$$

The reduced skin friction coefficient (Cf_X) and local Nusselt number (Nu_X) are respectively:

$$Cf_X = Cf(Ra_x)^{\frac{1}{4}} = A_5 Pr_f S''(0), \quad Nu_X = NuRa_x^{-\left(\frac{1}{4}\right)} = -\left(A_6 + \frac{4R}{3}\right)\theta'(0). \tag{5.2.17}$$

5.3 Numerical solution

The nonlinear ordinary differential system in Eqns. (5.2.11)-(5.2.12) with corresponding boundary conditions (5.2.13) are solved by employing the Runge-Kutta method of fourth-order with shooting technique. Refined values of initial guesses are found by the Newton-Raphson method with an accuracy of 10^{-6}. The domain of the present study is fixed to [0, 20] as a larger value for ∞ had no significant effect. Numerical values of the present study are compared with previously published results of (Kuznetsov & Nield, 2010) and (Mahanthesh & Mackolil, 2021) as described in Table 5.3. Furthermore, in Table 5.3, the results are also validated with the numerical results obtained by Fehlberg method and the bvp5c routine, a built-in solver in MATLAB. A commendable agreement of the present results with previously published results and the results from the bvp5c routine is noted. In addition, the numerical values of wall shear stress for various values of angle of inclination show an excellent agreement with bvp5c (see Table 5.4). To arrive at the numerical solutions, the following substitution is made:

$$S = y_1, S' = y_2, S'' = y_3, \theta = y_4, \theta' = y_5. \tag{5.3.1}$$

Accordingly, the equations (5.2.11)-(5.2.12) with boundary condition (5.2.13) takes the form as given below:

$$\begin{gathered} y_1^{'} = y_2, \\ y_2^{'} = y_3, \\ y_3^{'} = \frac{1}{4Pr_f}\frac{A_1}{A_5}\ \left(2(y_2)^2 - 3y_1y_3\right) - \frac{1}{A_5}\left\{A_3y_4 + A_1\alpha_1y_4^2\right\}\ cos\alpha + \frac{A_4}{A_5}My_2, \\ y_4^{'} = y_5, \\ y_5^{'} = \frac{-\frac{Q_E}{A_6}\exp(-m\zeta) - \frac{3}{4}\frac{A_2}{A_6}\ y_1y_5}{\left(1+\frac{4}{3}\frac{R}{A_6}\right)}, . \end{gathered} \tag{5.3.2}$$

with

$y_1(0) = 0, y_2(0) = 0, y_3(0) = K_1, y_4(0) = 1, y_5(0) = K_2.$

where, K_1 and K_2 are estimated using the Newton-Raphson method, a numerical procedure that aids in computing the roots of a real valued function. This method is governed by the idea that an analytic function can be estimated by approximating a straight-line tangent to it.

Table 5.3: *Comparison of $-\theta^{'}(0)$ values and when $\alpha_1 = \alpha = M = Q_E = R = 0$ and $\phi = 0$ with the results of (Kuznetsov & Nield, 2010) and (Mahanthesh & Mackolil, 2021)*

P_r	Kuznetsov & Nield	Mahanthesh & Mackolil	Present study		
			RK4	RKF45	Bvp5c
1	0.401	0.401	0.4010118	0.4010117	0.4010118
10	0.463	0.4633	0.4632903	0.4632903	0.4632903
100	0.481	0.4811	0.4810727	0.4810727	0.4810727
1000	0.484	0.4836	0.4836079	0.4836078	0.4836079

Table 5.4: *Comparison of $S''(0)$ when $\alpha_1 = 0.1, m = 0.5, M = 0.1$, $Q_E = 0.2, R = 1$ and $\phi = 1\%$*

α	Runge-Kutta method	bvp5c algorithm	Increment rate (%)
	$S''(0)$	$S''(0)$	
0^0	1.3974581543	1.3974581546	–
15^0	1.3597001912	1.3597001914	-2.7019
30^0	1.2472074728	1.2472074729	-8.2733
45^0	1.0619645094	1.0619645094	-14.8526
60^0	0.8056606724	0.8056606723	-24.1349
75^0	0.4742217598	0.4742217598	-41.1388
90^0	0.0000000000	0.0000000000	-100

5.4 Results and discussion

The impact of different parameters namely volume fraction of nanoparticles (ϕ), Hartmann number (M), quadratic thermal convection parameter (α_1), exponential heat source parameter (Q_E), radiation parameter (R), and exponential index (m) on velocity profile ($S'(\zeta)$), and temperature profile ($\theta(\zeta)$) of an inclined plate is explored through Figs. 5.2-5.9. The blue and red lines delineate the fluid flow past vertical and inclined plates respectively. A medium angle of inclination ($\alpha = 45^0$) has been chosen for the inclined plate case. The calculated value of the Prandtl number (Pr_f) for ethylene glycol (EG) at 300 K is 150.4583. The effect of differing inclination angles on drag force is tabulated in Table 5.4. It can be noticed that an increase in the angle of inclination exhibits a negative impact on the physical quantity. Further the rate (%) of decrements in wall shear stress is shown in Table 5.4. A decrement rate of 41.1388 % in wall shear stress is observed when the plate is inclined from 60^0 to 75^0. Physically, this occurs due to a depreciation in the fluid velocity (see (Goyal & Bhargava, 2018)).

Figs. 5.2-5.3 delineate the impact of the parameter ϕ on $S'(\zeta)$, and $\theta(\zeta)$ respectively. The liquid velocity retards by the augmented values of ϕ. The velocity profile starts from zero and attains a maximum peak then asymptotically converges to zero satisfying the conditions at the boundaries (see (Aziz & Khan, 2012)). Nanofluid flow past a vertical and an inclined plate cases are compared in this study. Nanoparticles tend to form aggregates (see (Chen et al., 2007)). Augmentation in the volume fraction of nanoparticles promotes more aggregation and enhances the viscosity of nanofluid which in turn depreciates the velocity profile. The temperature profile enhances by incremented values of ϕ. The addition of nanoparticles enhances the thermal conductivity of nanofluid (see (Chen et al., 2007),(Acharya, Das, & Kundu, 2019)) which raises the temperature profile. Figs. 5.4-5.5 display the variation of $S'(\zeta)$, and $\theta(\zeta)$ profiles with M. The distance covered by the nanofluid per unit time decreases when M is incremented. An increment in M induces a drag force (namely Lorentz force) against the fluid flow which decelerates the velocity profile (see (Goyal & Bhargava, 2018)). The temperature profile increases as shown in Fig. 5.5. This is due to an increase in friction. This is in agreement with findings of (Goyal & Bhargava, 2018). Figs 5.6-5.7 display the effect of α_1 on $S'(\zeta)$ and $\theta(\zeta)$

profiles. An increment in α_1 heightens the $S'(\zeta)$ profile. Physically, the enhancement in α_1 exhibits a force on the fluid due to a boost in the temperature gradient at the wall which accelerates fluid flow as a result of which the velocity increases and the temperature decreases.

Fig. 5.8 shows the influence of $\theta(\zeta)$ with increment in Q_E. $\theta(\zeta)$ rise with enhance in Q_E due to the presence of an additional heat source. Fig. 5.9 illustrates the trend of $\theta(\zeta)$ with R. $\theta(\zeta)$ improves with an increase in R. An increment in R applies more heat flux on the fluid and therefore, the temperature of the fluid enhances (see (L. Zhang et al., 2021)). The trend of fluid flow over both vertical and inclined plates is qualitatively similar but a greater velocity profile is observed in the case of the fluid flow over a vertical plate. It is because the buoyancy force exerted on the fluid past an inclined plate is much higher than that on the vertical plate. It is also inferred from these figures that, the temperature of the nanofluid is increasing functions of α.

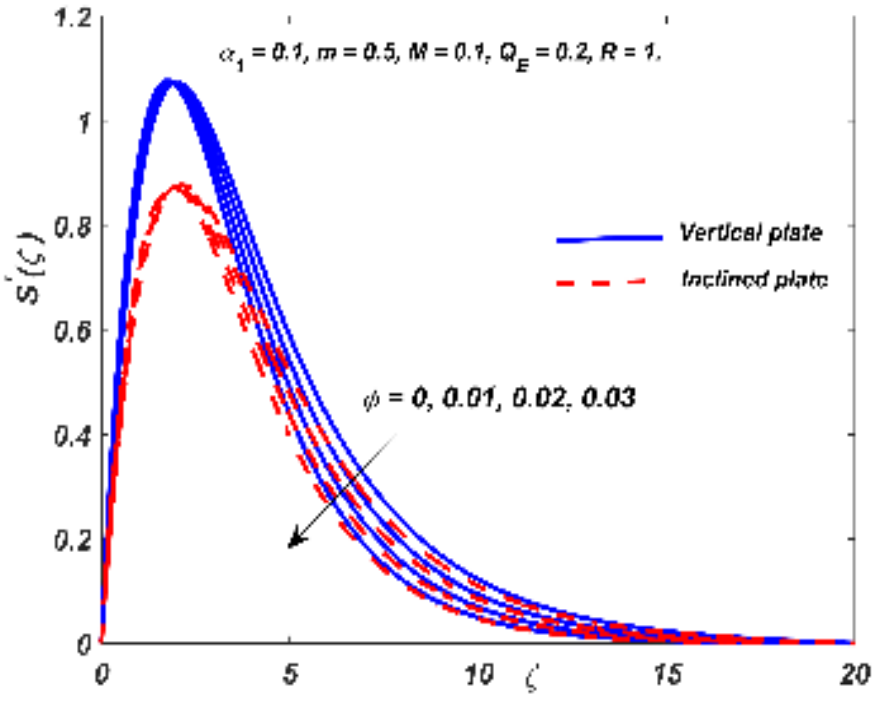

Figure 5.2: *Variation of $S'(\zeta)$ for distinct values of ϕ.*

Figs. 5.10 to 5.13 illustrate the simultaneous effects of pertinent parameters on the dependent variable studied. The change in the skin friction coefficient Cf_X with variations in α_1 and ϕ is described in Fig. 5.10. It can be observed that Cf_X is

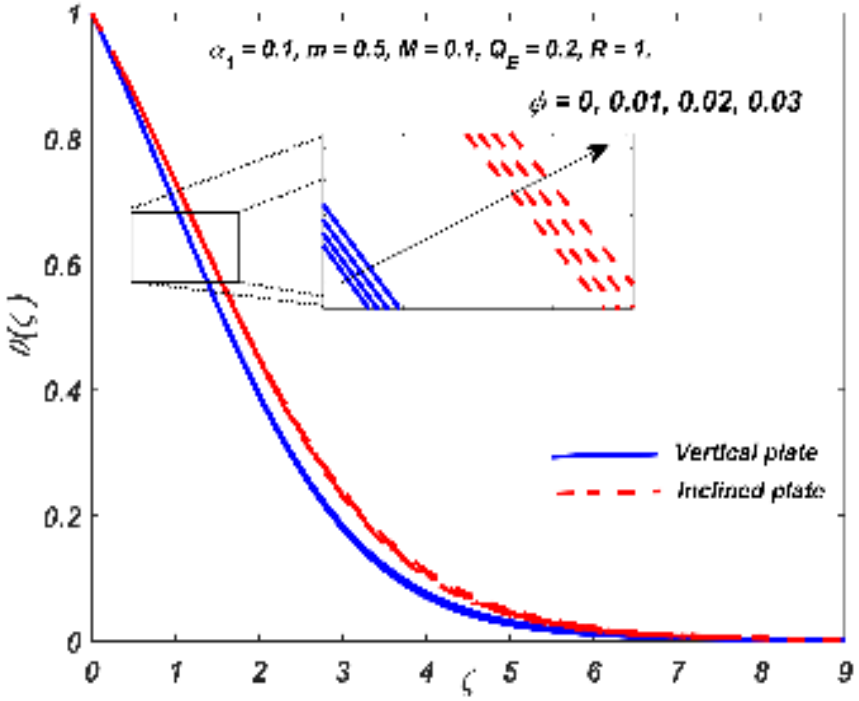

Figure 5.3: *Variation of $\theta(\zeta)$ for distinct values of ϕ.*

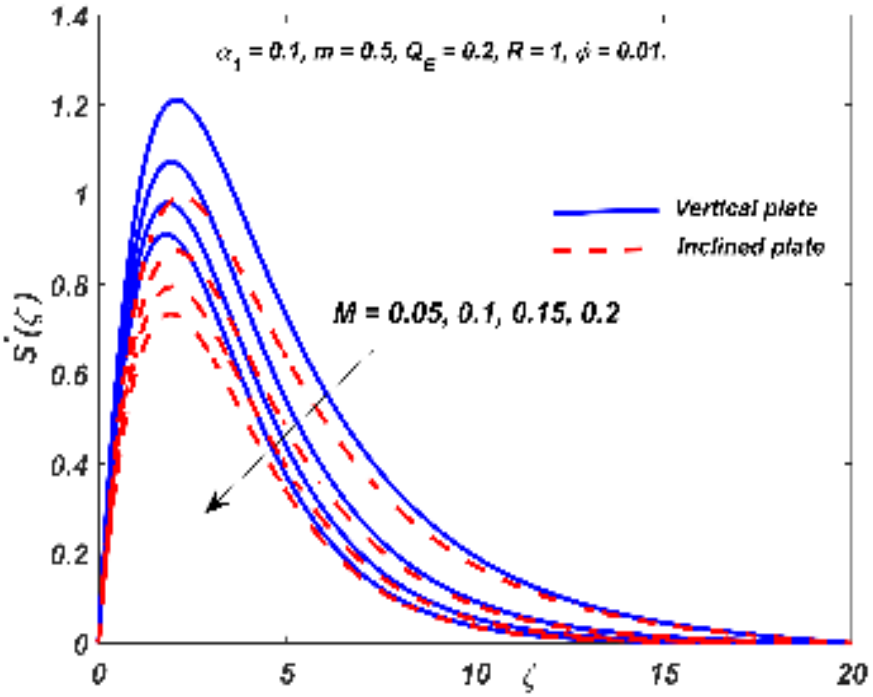

Figure 5.4: *Variation of $S'(\zeta)$ for distinct values of M.*

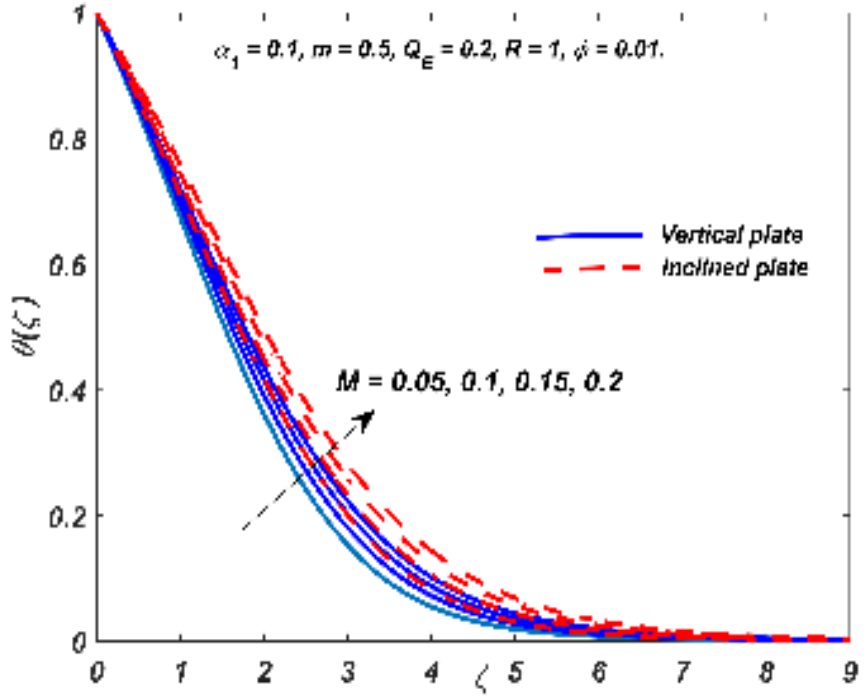

Figure 5.5: *Variation of $\theta(\zeta)$ for distinct values of M.*

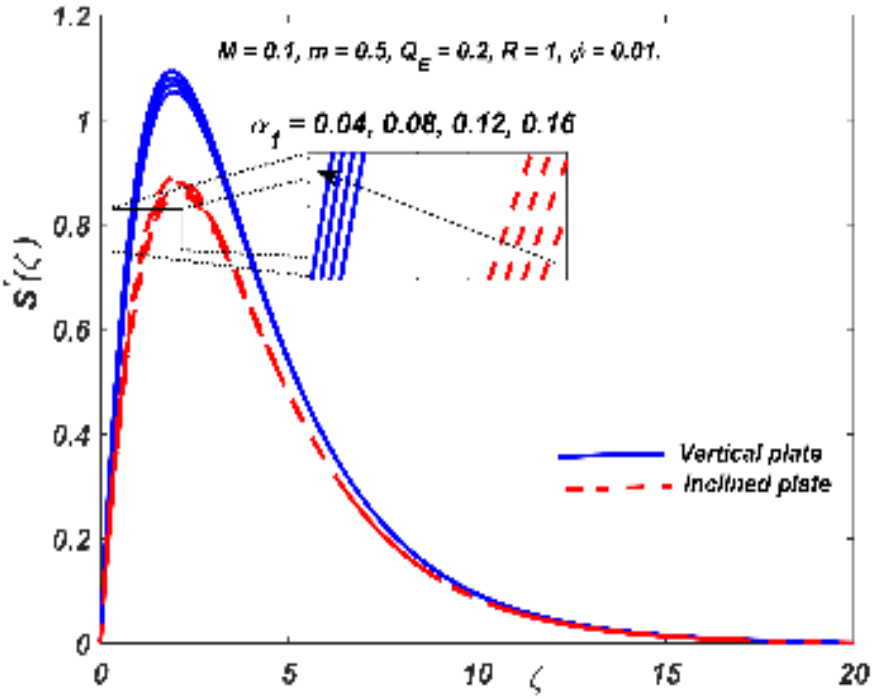

Figure 5.6: *Variation of $S'(\zeta)$ for distinct values of α_1.*

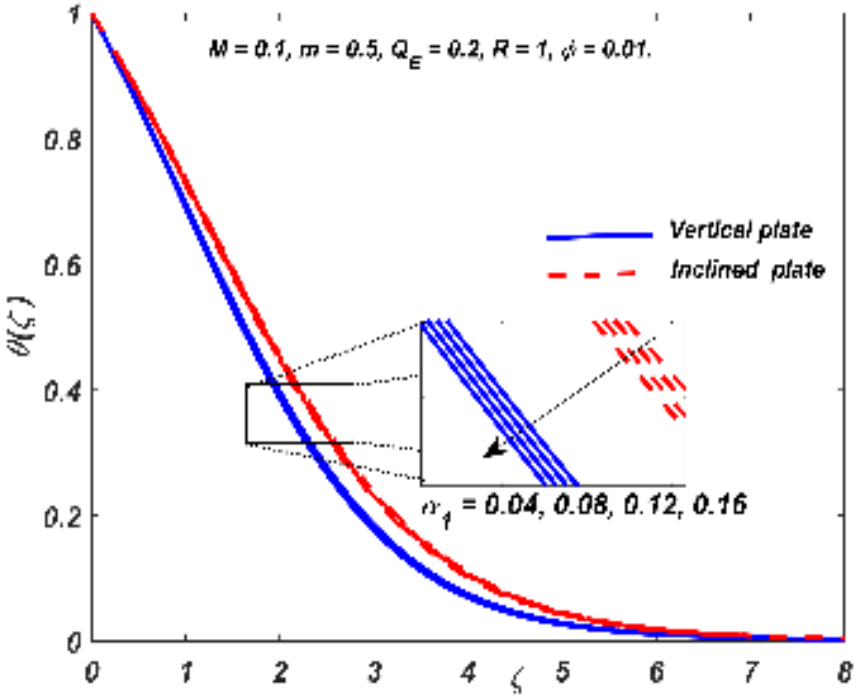

Figure 5.7: *Variation of* $\theta(\zeta)$ *for distinct values of* α_1.

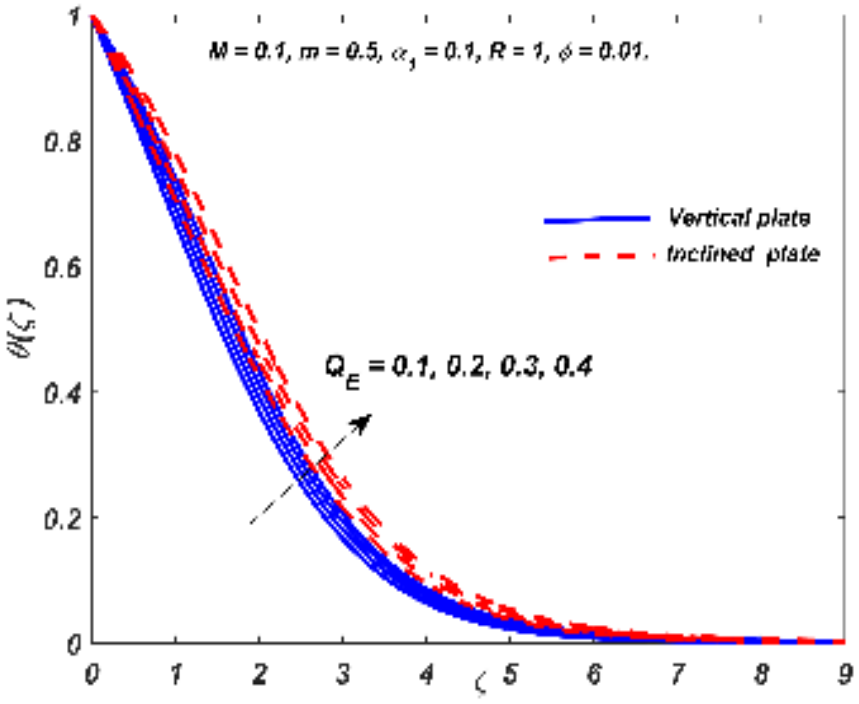

Figure 5.8: *Variation of* $\theta(\zeta)$ *for distinct values of* Q_E.

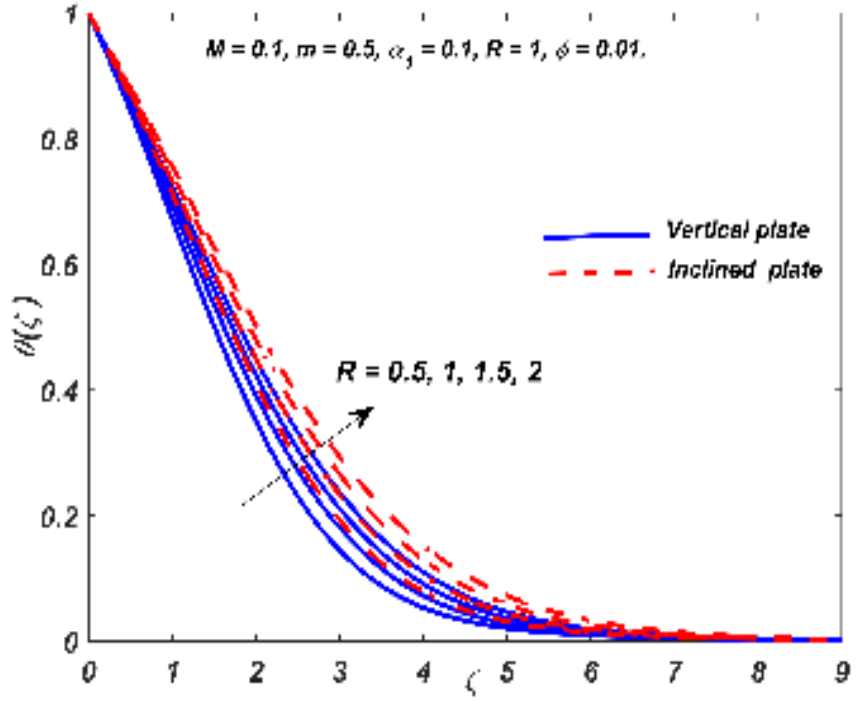

Figure 5.9: *Variation of $\theta(\zeta)$ for distinct values of R.*

an increasing function of α_1 and a decreasing function of ϕ. Maximum drag force is obtained at minimum α and M values as shown in Fig. 5.11. Physically, this is due to the effect of Lorentz and buoyancy forces near the surface. Fig. 5.12 delineates the influence of α and M on the heat transfer coefficient. It can be seen that the heat flux has a relatively small change by the increase in α and M. The heat transfer attains maximum for low values of α and M. (see (Acharya, Das, & Kundu, 2018)).Fig. 5.13 shows the variation in heat transfer with an increase in α_1 and ϕ. Maximum heat flux is observed for high α_1 and ϕ values.

5.5 Response Surface Methodology (RSM)

The RSM is a statistical and mathematical design-based tool to explore the interactive impact of pertinent parameters on a response variable of interest and to optimize it. Here, a full quadratic model is considered as follows:

$$\begin{aligned} Response = \chi_1 X_1 + \chi_2 X_2 + \chi_3 X_3 + \chi_4 X_1 X_2 + \chi_5 X_1 X_3 + \chi_6 X_2 X_3 \\ + \chi_7 X_1^2 + \chi_8 X_2^2 + \chi_9 X_3^2 + \chi_{10}. \end{aligned} \tag{5.5.1}$$

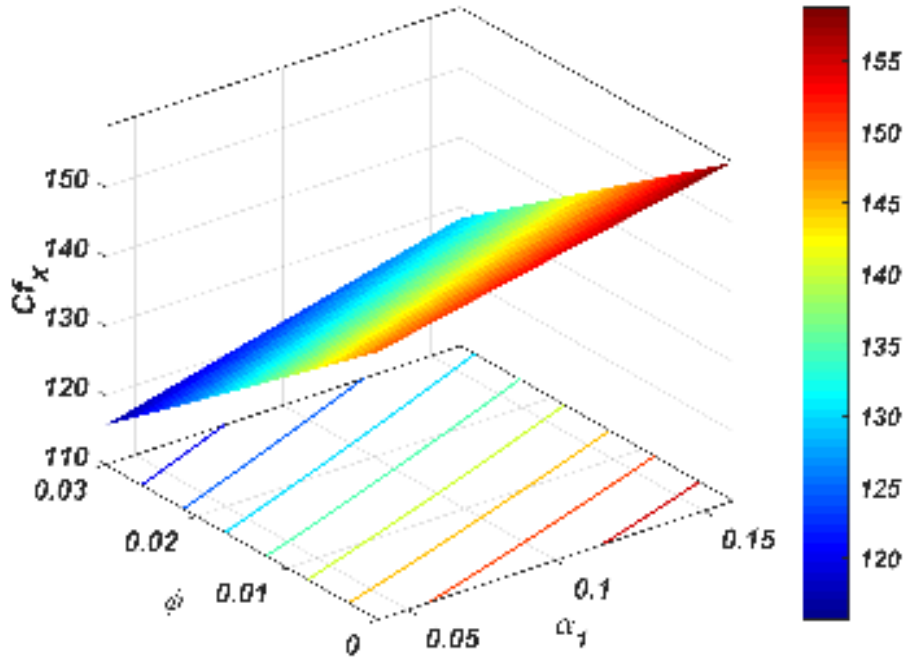

Figure 5.10: *Surface plot of Cf_X for variation of α_1 and ϕ .*

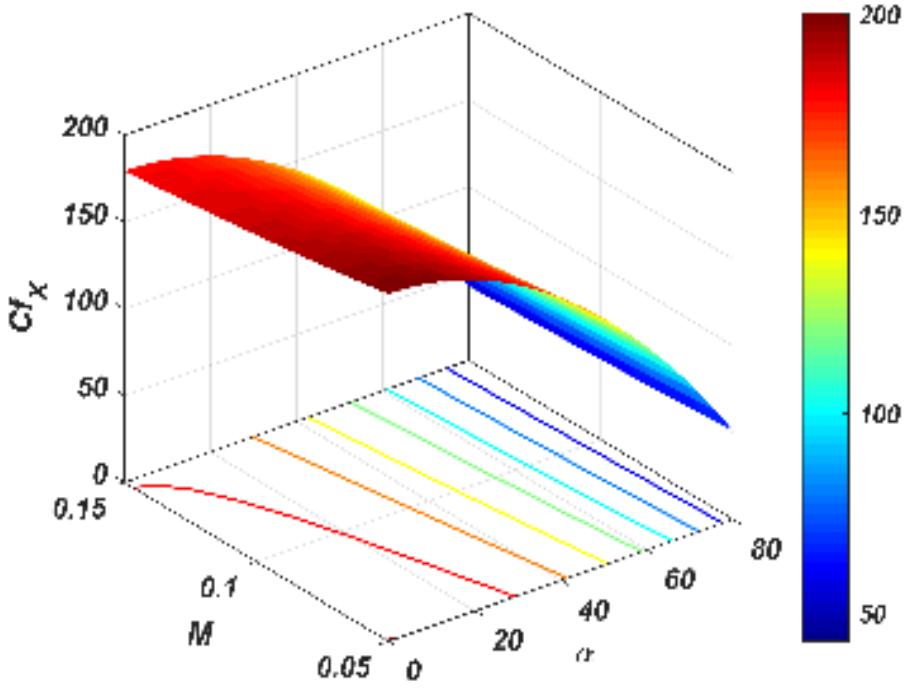

Figure 5.11: *Surface plot of Cf_X for variation of α and M*

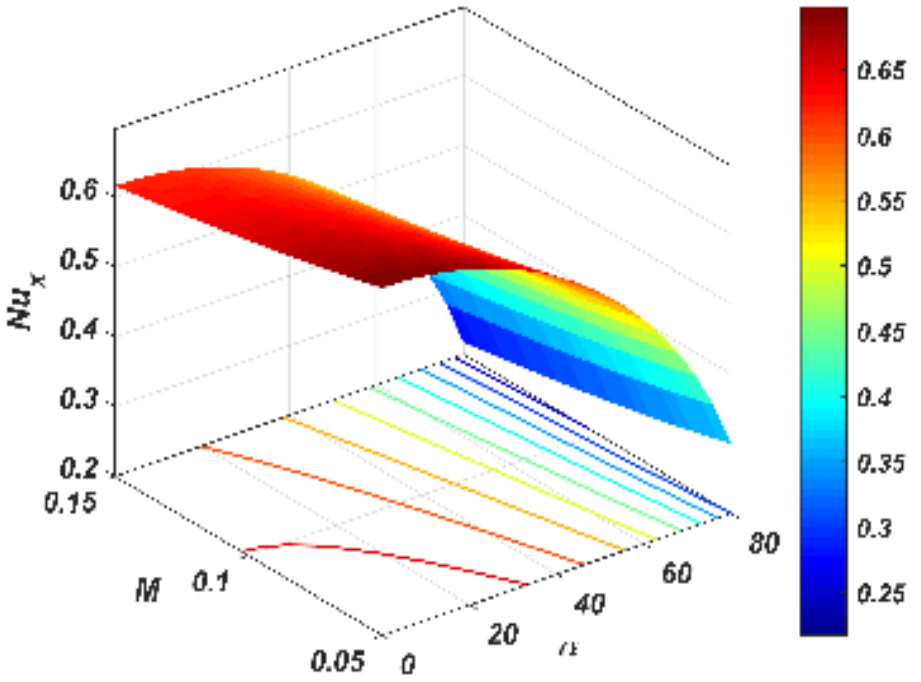

Figure 5.12: *Surface plot of Nu_X for variation of α and M .*

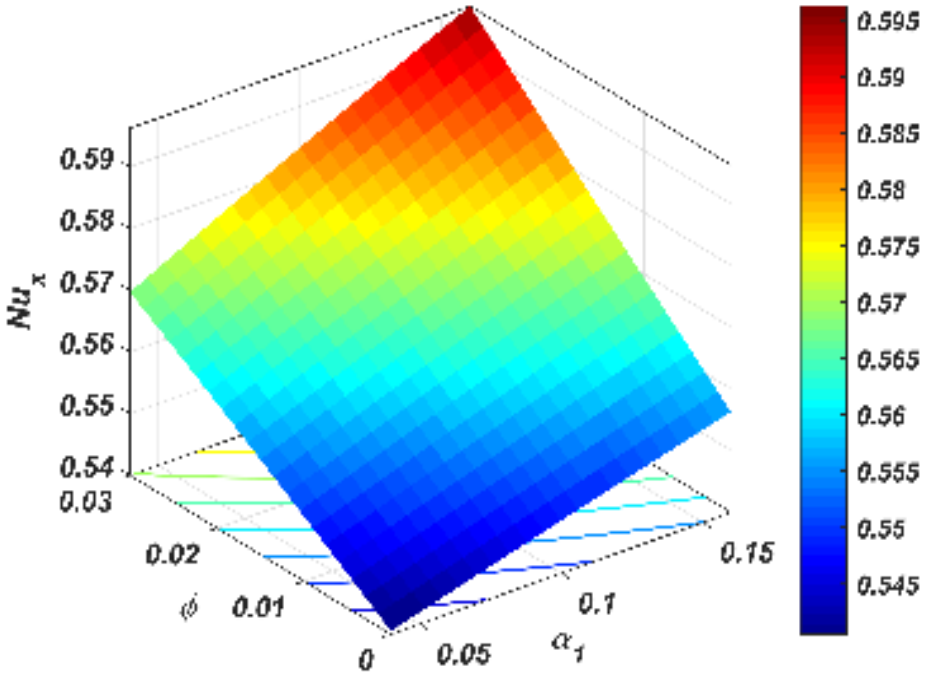

Figure 5.13: *Surface plot of Nu_X for variation of α_1 and ϕ .*

Table 5.5: *The effective levels of parameters*

Parameters	Coded Symbols	Levels		
		-1 (Low)	0 (Medium)	1 (High)
α	X_1	30^0	45^0	60^0
Q_E	X_2	0.15	0.2	0.25
R	X_3	0.8	1	1.2

Here, χ_i denotes the regression coefficients. The parameters α $\left(30^0 \leq \alpha \leq 60^0\right)$, Q_E $(0.15 \leq Q_E \leq 0.25$) and R $(0.8 \leq R \leq 1.2)$ are inducted for the analysis. Heat transfer coefficient (Nu_X) is the response variable. Here, a face-centered central composite design (CCD) is adopted for interpreting the influence of parameters on the response variable. The statistical technique involves 20 runs based on the face (P)- factor (F) relation $(2^F + 2F + P)$. It contains 8 factorial, 6 axial, and 6 centre points. The parameters α, Q_E and R are coded as X_1, X_2, and X_3 respectively. The effective levels of parameters are described in Table 5.5. Fig. 5.14 shows the precision

Table 5.6: *ANOVA table*

Source	**Deg. of Freedom**	**Adj. Sum of Squares**	**Adj. Mean Squares**	**F-value**	**p-value**
Model	9	0.107255	0.011917	46593.65	< 0.001
Linear terms	3	0.10564	0.035213	137676.2	< 0.001
α	1	0.047442	0.047442	185487.28	< 0.001
Q_E	1	0.026774	0.026774	104680.6	< 0.001
R	1	0.031424	0.031424	122860.73	< 0.001
Square terms	3	0.00137	0.000457	1784.96	< 0.001
α^2	1	0.000712	0.000712	2781.96	< 0.001
Q_E^2	1	0	0	0.14	**0.713**
R^2	1	0.000002	0.000002	8.11	0.017
Interaction terms	3	0.000245	0.000082	319.77	< 0.001
$\alpha.Q_E$	1	0.000031	0.000031	120.82	< 0.001
$\alpha.R$	1	0.000208	0.000208	811.71	< 0.001
$Q_E.R$	1	0.000007	0.000007	26.79	< 0.001
Errors	10	0.000003	0		
Lack-of-Fit	5	0.000003	0.000001	*	*
Pure Error	5	0	0		
Total	19	0.107258			
Coefficient of determination $\mathcal{R}^2 = 99.98\%$					

of the model. It is observed from the normal probability plot that data points are aligned along a straight line. The bell-shaped residual histogram concludes that residuals follow a normal distribution. The magnitude of residual against the fitted value and the residual against observation order plots are less than 0.001. It can be observed from the ANOVA table in Table 5.6 that the square term of Q_E is not significant as the p value is greater than 0.05. The coefficient of determination ($\mathcal{R}^2$) computes the variation in the response variable as explained by the independent variables taken in the model. It also explains the accuracy of the model. Here, $\mathcal{R}^2$ is found to be 99.98% and it guarantees the accuracy of the model.

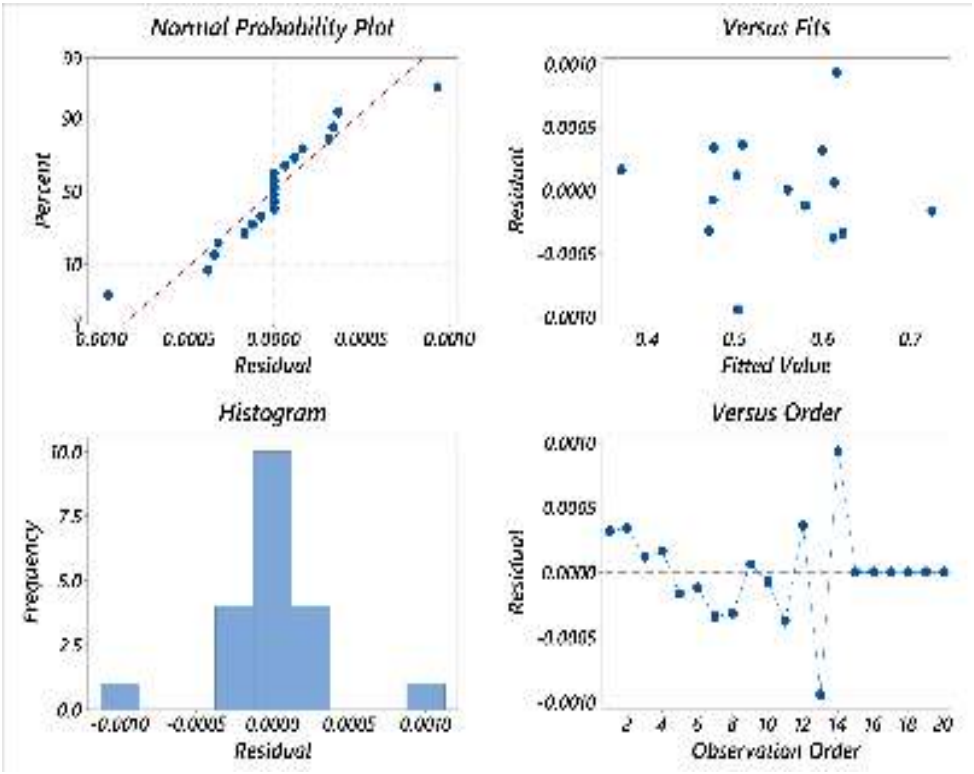

Figure 5.14: *Residual plots for Nu_X.*

5.5.1 Statistical Analysis

The full quadratic model for the wall heat flux by considering uncoded parameter values are

$$Nu_X = 0.41028 + 0.004064\ \alpha - 0.8429\ Q_E + 0.4186\ R - 0.000071\ \alpha^2 - 0.02171\ R^2 - 0.002621\ \alpha Q_E - 0.001698\ \alpha R - 0.0925\ Q_E R \tag{5.5.2}$$

The above relation can be used to estimate Nu_X accurately for the parameters in the given ranges. Fig. 5.15 (a) to (f) display the simultaneous impact of parameters on the heat transfer coefficient utilizing contour and surface plots. Variation in heat transfer coefficient with two parameters is considered by holding the third parameter at the medium level. It can be inferred from Fig. 5.15 (a)-5.15(b) that an increment in α reduces Nu_X also, Nusselt number is maximum for low values of α and Q_E. The Nusselt number with variation in R and α and R and Q_E is described in Figs. 5.15 (c) to 5.15 (f) respectively. These figures illustrate that the heat transfer coefficient is a decreasing function of α and an increasing function of R and similar trends are observed for Q_E and R. The interactive effects on the heat transfer coefficient can also be observed from Fig. 5.15.

5.6 Sensitivity analysis

The sensitivity of the heat flux is computed by using the coded coefficients of the full quadratic model as given below.

$$Nu_X = 0.560098 - 0.068878\ X_1 - 0.051744\ X_2 + 0.056057\ X_3 - 0.016085\ X_1^2 - 0.000868\ X_3^2 - 0.001965\ X_1X_2 - 0.005094\ X_1X_3 - 0.000925\ X_2X_3 \tag{5.6.1}$$

Sensitivity functions are estimated by computing the partial derivatives in a full quadratic model concerning the coded variables as follows:

$$\frac{\partial Nu_X}{\partial X_1} = -0.068878 - 0.03217\ X_1\ - 0.001965\ X_2 - 0.005094\ X_3, \tag{5.6.2}$$

$$\frac{\partial Nu_X}{\partial X_2} = -0.051744 - 0.001965\ X_1 - 0.000925\ X_3, \tag{5.6.3}$$

$$\frac{\partial Nu_X}{\partial X_3} = 0.056057 - 0.001736\ X_3 - 0.005094\ X_1 - 0.000925\ X_2. \tag{5.6.4}$$

The sensitivity of the heat transfer coefficient is visualized using bar chart (see Figure 5.16). The nature of the sensitivity is indicated by a positive or negative sign which means that the response term is positively or negatively correlated with the change in the effective parameter values. The magnitude of sensitivity indicates the intensity of this relationship. Here, the sensitivity of heat transfer coefficient (Nu_X) is computed by assuming a medium inclination angle ($\alpha = 45°$). Table 5.7 and Fig. 5.16 explains the sensitivities of Nu_X at different effective parameter levels.

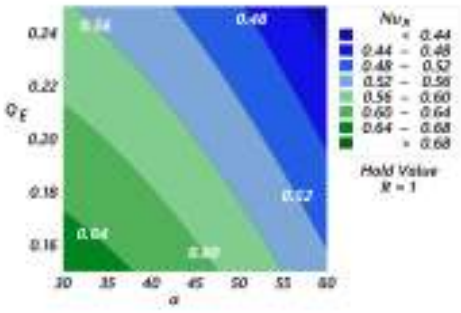

(a) *Contour plot of Nu_X for variation of α and Q_E*

(b) *Response surface plot of Nu_X for variation of α and Q_E*

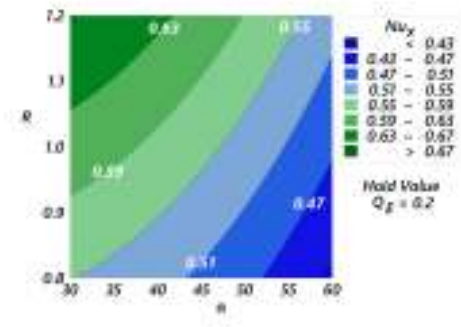

(c) *Contour plot of Nu_X for variation of α and R*

(d) *Response surface plot of Nu_X for variation of α and R*

Figure 5.15: *Contour plots and Response surface plots of Nu_X for all combinations of α, Q_E and R.*

Nu_X is negative sensitive towards α, Q_E and positive sensitive towards R. For a fixed value of Q_E at the low level ($X_2 = -1$) the magnitude of the sensitivity of Nusselt number enhances towards α and Q_E with an increment in the level of R whereas the sensitivity magnitude towards R reduces. A similar trend is noted for the medium and high levels of X_2. Further, the sensitivity towards α is more when compared to Q_E and R (due to the highest sensitivity magnitude). Additionally, the augmentation rate of the sensitivity magnitude for incrementing the levels of R are tabulated in the Table 5.7. This provides the rate at which the sensitivity is augmented for varying the levels of R which led to the following results:

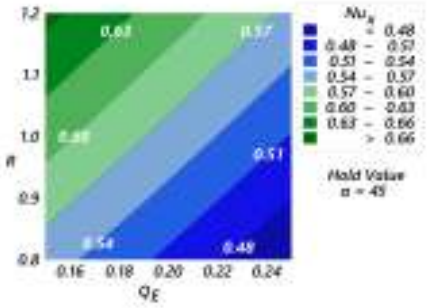

(e) *Contour plot of Nu_X for variation of Q_E and R*

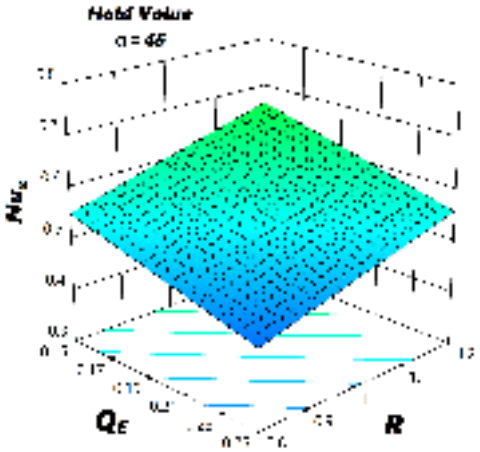

(f) *Response surface plot of Nu_X for variation of Q_E and R*

Figure 5.15: *Contour plots and Response surface plots of Nu_X for all combinations of α, Q_E and R.*

Table 5.7: *The sensitivity values of the response Nu_X when $X_1 = 0$*

B	C	Sensitivity values		
		$\frac{\partial Nu_X}{\partial X_1}$	$\frac{\partial Nu_X}{\partial X_2}$	$\frac{\partial Nu_X}{\partial X_3}$
-1	-1	-0.061819	-0.050819	0.058718
	0	-0.066913	-0.051744	0.056982
	1	-0.072007	-0.052669	0.055246
Rate of change		0.005094	0.000925	-0.001736
0	-1	-0.063784	-0.050819	0.057793
	0	-0.068878	-0.051744	0.056057
	1	-0.073972	-0.052669	0.054321
Rate of change		0.005094	0.000925	-0.001736
1	-1	-0.065749	-0.050819	0.056868
	0	-0.070843	-0.051744	0.055132
	1	-0.075937	-0.052669	0.053396
Rate of change		0.005094	0.000925	-0.001736

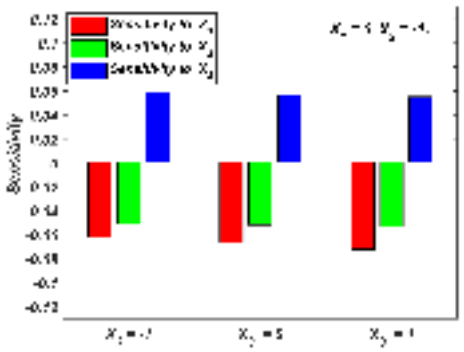

(a) *Bar charts depicting the sensitivity of Nu_X with $X_2 = -1$*

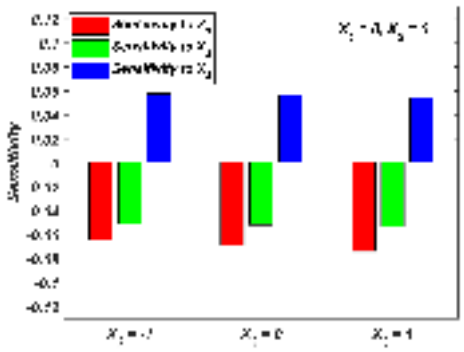

(b) *Bar charts depicting the sensitivity of Nu_X with $X_2 = 0$*

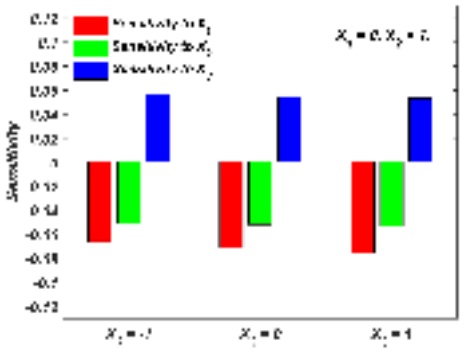

(c) *Bar charts depicting the sensitivity of Nu_X with $X_2 = 1$*

Figure 5.16: *Bar charts depicting the sensitivity of Nu_X with $X_2 = -1$,$X_2 = 0$,and $X_2 = 1$*

- The sensitivity towards α changes at the rate 0.5094
- The sensitivity towards Q_E changes at the rate 0.0925
- The sensitivity towards R changes at the rate -0.1736

This implies that the interactive effect on heat flux by the angle of inclination is predominant.

5.7 Conclusions

The hydromagnetic nanofluid flow past an inclined plate is explored with aggregation kinematics and significant buoyancy forces. The Runge-Kutta-based shooting method is adopted for the numerical computations. The limiting case of the present problem was found to be in good agreement with the literature. Sensitivity analysis based on the Response Surface model was conducted for a detailed study of the wall heat

flux. The present study includes potential applications in flat plate solar collectors and heat exchangers. The major conclusions of the present work are as given below:

- The aggregation kinematic aspect enhances the temperature field due to the improved thermal conductivity of the nanofluid.
- The velocity retards due to variation in Hartmann number and an opposite trend is exhibited for temperature. It is due to the generated opposing force, namely the Lorentz force.
- The temperature profile enhances with more thermal radiation and exponential heat source effects. Physically, these parameters contribute more energy to the fluid
- The surface drag force is an increasing function of quadratic thermal convection aspect.
- Maximum heat transfer occurs at the highest level of quadratic thermal convection and nanoparticle volume fraction parameters.
- The heat flux is more sensitive to the inclination angle when compared to other parameter values. This sensitivity augments at a rate 0.5094% for the increment in R.
- An accurate quadratic model is estimated for the wall heat flux with $\mathcal{R}^2 =$ 99.98%.
- The wall shear stress decrements by 41.1388 % when the inclination of the plate is changed from 60^0 to 75^0.

This work can be further explored by the inclusion of dissipation effects and the utilization of a suitable non-Newtonian fluid model, based on the practical applicability.